Anharmonicity-induced phonon hardening and phonon transport enhancement in crystalline perovskite $BaZrO_3$

Jiongzhi Zheng,[1] Dongliang Shi,[2] Yuewang Yang,[1] Chongjia Lin,[1] He Huang,[1] Ruiqiang Guo,[3,*] and Baoling Huang[1,4,†]

[1]*Department of Mechanical and Aerospace Engineering, The Hong Kong University of Science and Technology, Clear Water Bay, Kowloon, Hong Kong*

[2]*Department of Land Surveying and Geo-Informatics, The Hong Kong Polytechnic University, Hung Hom, Kowloon, Hong Kong*

[3]*Thermal Science Research Center, Shandong Institute of Advanced Technology, Jinan, Shandong Province, 250103, China*

[4]*HKUST Shenzhen-Hong Kong Collaborative Innovation Research Institute, Futian, Shenzhen, 518055, China*

(Received 11 August 2021; revised 18 May 2022; accepted 20 May 2022; published 7 June 2022)

We investigated the effects of cubic and quartic anharmonicity on lattice dynamics and thermal transport in highly anharmonic $BaZrO_3$ crystal over a wide temperature range (300–2000 K) by combining the first-principles-based self-consistent phonon theory and a unified theory of thermal transport including population and coherence contributions. By considering the effects from bubble and loop diagrams, the contributions of both three-phonon (3ph) and four-phonon (4ph) interaction processes to phonon scattering rates and energy shifts were clarified. Anharmonic phonon renormalization is found to play a crucial role in determining the finite-temperature phonon energies and lattice thermal conductivity κ_L in $BaZrO_3$. Specifically, the lattice anharmonicity induces significant low-frequency optical phonon hardening at elevated temperatures, which is correlated with the U-shaped potential energy surfaces for these modes. The low-frequency optical phonon hardening significantly suppresses phonon scattering rates by altering the phonon weighted phase space of both 3ph and 4ph interaction processes, thereby leading to significant enhancement in the κ_L and weaker temperature dependence of $\kappa_L \sim T^{-0.75}$ than traditional harmonic treatments. Moreover, although the coherent thermal transport channel is suppressed by anharmonic phonon renormalization, it is enhanced by the 4ph scattering processes. The coherence contribution becomes nonnegligible at elevated temperatures and may contribute up to 17.38% of the total κ_L at 1500 K. In this paper, we highlight the strong influence of the lattice anharmonicity on thermal conductivity in severely anharmonic systems and the importance of coherent thermal transport channel at elevated temperatures.

DOI: 10.1103/PhysRevB.105.224303

I. INTRODUCTION

Ternary perovskite-type oxides, of the general chemical formula ABO_3, where A and B denote different metal ions, are a large family of materials possessing cubic, rhombohedral, orthorhombic, tetragonal, and monoclinic phases [1]. Among them, barium zirconate ($BaZrO_3$) is a perovskite oxide with a cubic structure, as shown in Fig. 1(a). Recently, it has drawn vast attention not only for fundamental research but also for practical application due to its outstanding physical properties, such as excellent thermal stability, high melting point, small thermal expansion coefficient, low dielectric loss, and low thermal conductivity [2,3], which can benefit a broad range of applications such as high-temperature crystal growth [4], high-temperature fuel cells [5,6], safety engineering [7], and thermal barrier coatings for gas turbines [8,9]. In many of these applications, the lattice thermal conductivity κ_L of $BaZrO_3$ plays a key role. Several theoretical studies based on the classical molecular dynamics (MD) [10] or first-principles approach [11] have been performed to predict the κ_L of $BaZrO_3$ but could not capture its weak temperature dependence [9,11,12]. Accurate prediction of the κ_L in $BaZrO_3$ remains a challenge. Specifically, the first-principles studies based on harmonic approximation (HA) phonon theory remarkably underestimated the phonon energy and κ_L in $BaZrO_3$ crystal at high temperatures [11]. Similar underestimation of κ_L within the HA framework is fairly common for oxide and fluoride perovskites such as $BaHfO_3$, $SrTiO_3$, $KZnF_3$, and $KMgF_3$ [13].

Going beyond the HA model, authors of recent studies have investigated anharmonic effects as the possible origin of the abovementioned discrepancy in some highly anharmonic crystals [14–16], finding that lattice anharmonicity plays a crucial role in quantifying the finite phonon linewidth and thermal conductivity κ_L [17]. However, prediction of lattice dynamics and phonon transport in materials of strong anharmonicity persists as one of the longstanding challenges in condensed matter physics [17–20]. The conventional Peierls-Boltzmann picture of phonon transport is valid for well-defined phonon modes [21]; however, it was recently found to fail in describing the thermal transport in highly anharmonic crystals [14,22,23]. To overcome the shortcomings of the Peierls-Boltzmann picture of phonon transport, recently, the finite-temperature treatment of phonons induced

*ruiqiang.guo@iat.cn
†mebhuang@ust.hk

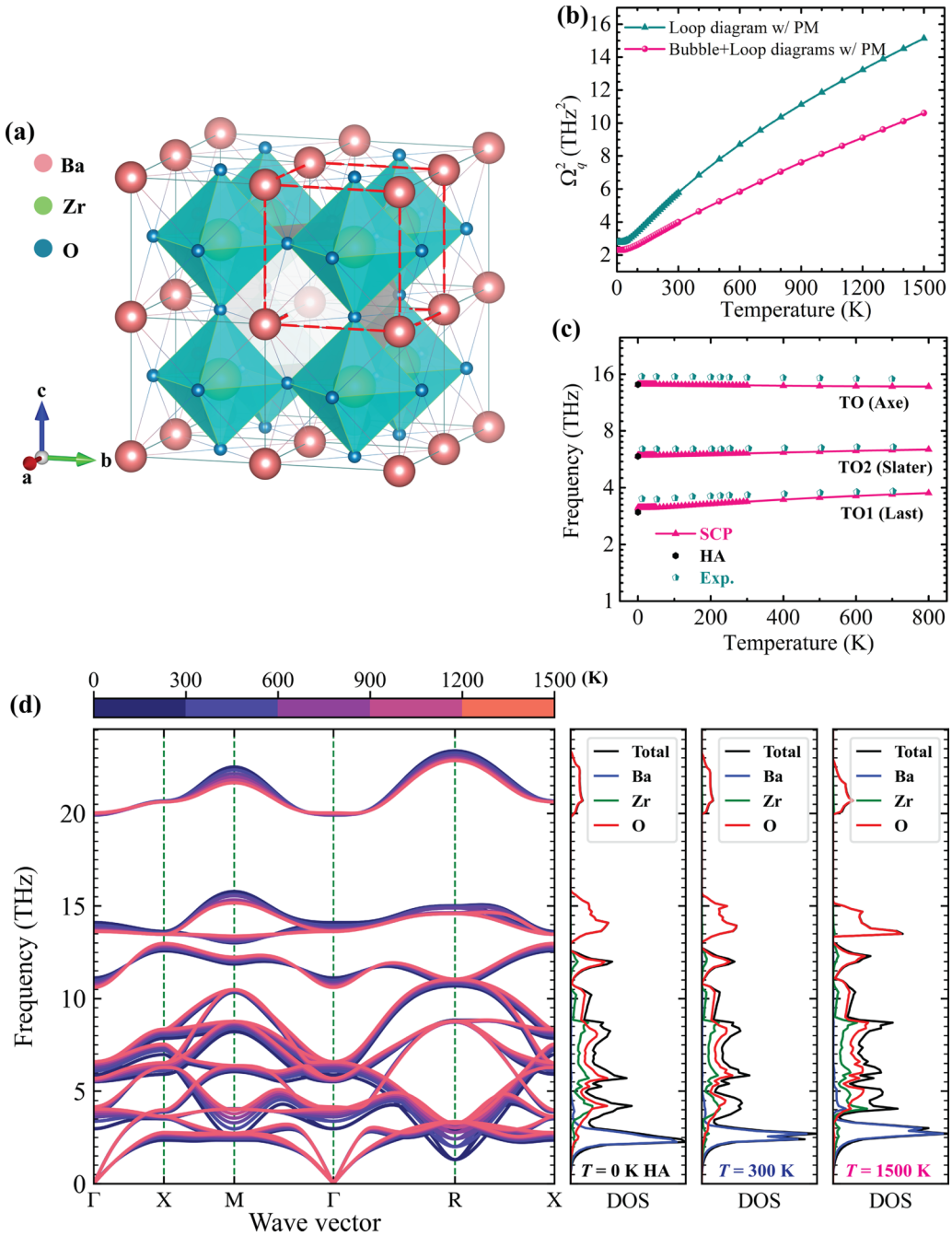

FIG. 1. (a) A $2 \times 2 \times 2$ supercell of $BaZrO_3$ crystal, which features a sublattice formed by ZrO_6 octahedra units together with Ba atoms. The red dash lines depict a lattice unit cell and Ba, Zr, and O atoms are colored in red, green, and blue, respectively. (b) Calculated temperature-dependent squared phonon frequency of R_{25} mode using the first-order self-consistent phonon (SCP) method (loop diagram) with polarization mixing (PM) compared with that further including the bubble diagram based on nonperturbative method, respectively. (c) Calculated temperature-dependent optical phonon frequencies at the Γ point in comparison with harmonic approximation (HA) results and experimental values [52]. (d) Calculated harmonic phonon dispersion at $T = 0$ K in comparison with the anharmonic phonon dispersions calculated at finite temperatures (300–1500 K). Atom-decomposed partial and total phonon densities of states at $T = 0$ (HA), 300, and 1500 K are shown on the right panel.

by lattice anharmonicity [17,18] and wavelike interbranch tunneling of coherence arising from off-diagonal terms of the heat flux operator [23] were proposed to explain experimental findings. Most efforts have been concentrated on anomalous thermal transport, i.e., ultralow thermal conductivity in highly anharmonic compounds with large complex unit cells [15,16,23]. However, simple crystals with strong anharmonicity, such as many ternary perovskite-type oxides, receive much less attention, [17,24–26] and a thorough and fundamental understanding of thermal transport in these simple but highly anharmonic crystals is to be developed.

In this paper, we investigate the effects of both cubic and quartic lattice anharmonicity on lattice dynamics and thermal transport in crystalline $BaZrO_3$ over a wide

temperature range (300–2000 K) using first-principles-based self-consistent phonon (SCP) calculations and a unified theory of thermal transport incorporating the population and coherence contributions. Here, a comprehensive treatment of thermal transport theory with the inclusion of isotope-phonon, three-phonon (3ph), and four-phonon (4ph) scatterings; anharmonic phonon renormalization from cubic and quartic anharmonicity; and phonon and coherent thermal transport channels is employed to predict the lattice thermal conductivity κ_L in crystalline $BaZrO_3$. We observe significant phonon hardening of low-frequency optical modes with increasing temperature due to the strong anharmonicity, which can suppress the 3ph and 4ph weighted phase space (WPS). The phonon hardening leads to significantly enhanced κ_L with weak temperature dependence in crystalline $BaZrO_3$. Good agreements between the calculated and measured κ_L in $BaZrO_3$ over a wide temperature range can be achieved by considering phonon frequency shifts from both the cubic and quartic anharmonicities and higher-order phonon scattering processes, highlighting the importance of cubic and quartic anharmonicity in determining the lattice dynamics and thermal transport in the simple anharmonic crystals, particularly at elevated temperatures. Furthermore, the coherence contribution ascribing from the off-diagonal terms of the heat flux operators becomes nonnegligible and improves the predicted results at high temperatures.

II. METHODOLOGY

In this paper, the density functional theory (DFT) calculations [27] were performed using the Vienna *Ab initio* Simulation Package (VASP) [28], where the projector augmented wave [29] pseudopotentials were employed to treat the Ba ($5s^25p^66s^2$), Zr ($4s^24p^65s^24d^2$), and O ($2s^22p^4$) shells as valence states. The Perdew-Burke-Ernzerhof (PBE) [30] of the generalized gradient approximation [31] was employed for the exchange-correlation functional in all DFT calculations. The PBE functional was selected here, as it could accurately reproduce many lattice properties including the lattice stability at low temperatures, while other functionals such as local-density approximation failed [32]. The hybrid functional, i.e., HSE and CX0p, may be more accurate [33], but the high computational cost makes it almost prohibitive to use to calculate thermal transport properties. A kinetic energy cutoff value of 600 eV and $10 \times 10 \times 10$ Monkhorst-Pack κ-point grids were applied to the Brillouin zone integration for structural optimization, with a tight convergence criterion of 10^{-7} eV Å^{-1} for the Hellman-Feynman forces acting on each atom, and 10^{-8} eV for the total energy. The optimized lattice is of a $Pm\bar{3}m$ space group (No. 221) with a lattice constant of $a = 4.235$ Å, in good agreement with the experimental values ($a = 4.193$ Å) [32] for $BaZrO_3$ single crystal. The nonanalytic part of the dynamical matrix was considered in all the following calculations. The Born effective charges Z and the dielectric tensor ε of $BaZrO_3$ were calculated using the density functional perturbation theory [34], and the obtained values [$\varepsilon^{\infty} = 4.843$, $Z^*(\mathrm{Ba}) = 2.742$, $Z^*(\mathrm{Zr}) = 6.146$, $Z^*(\mathrm{O})_{\perp} = -4.896$, and $Z^*(\mathrm{O})_{\mathrm{II}} = -1.997$] agree well with the previous computational results [35].

After the structural optimization, the finite displacement approach [36] was applied to obtain the harmonic interatomic force constants (IFCs) of a $3 \times 3 \times 3$ supercell containing 135 atoms, where the κ-point grids for the Brillouin zone integration were changed to $3 \times 3 \times 3$ to be commensurate with the supercell dimensions. In addition, $2 \times 2 \times 2$ supercells containing 40 atoms were used for mapping out the potential energy surfaces (PESs) with $5 \times 5 \times 5$ κ-point grids and 600 eV cutoff energies. Instead of using the conventional finite-displacement approach [36] to obtain the higher-order IFCs, we employed the compressive sensing lattice dynamics method, which applies the compressive technique [37] to collect the physically important terms in anharmonic IFCs based on the limited precise displacement-force datasets [17]. To generate the physically relevant atomic displacements, *ab initio* MD (AIMD) simulations were performed for a $3 \times 3 \times 3$ supercell system at 500 K with a $2 \times 2 \times 2$ Monkhorst-Pack κ-point grid, and a convergence criterion of electronic self-consistent field cycles of 10^{-5} eV was used to accelerate the structural sampling. The AIMD simulations were conducted for 3000 time steps in the NVT ensemble using a Nosé-Hoover thermostat and a 2 fs time step. We then sampled 100 atomic structures that were equally spaced in time by skipping the first 500 steps from the trajectories. We further displaced all the atoms for all the samples by 0.1 Å in random directions to decrease cross-correlations between the sampled configurations. To prepare the displacement-force datasets, we performed precise static DFT calculations with $3 \times 3 \times 3$ κ-point grids and the total energy convergence criterion of 10^{-8} eV for the 100 configurations obtained. Finally, based on the datasets comprising displacements and forces of the 100 quasirandom configurations, the anharmonic IFCs were fitted using the least absolute shrinkage and selection operator technique [38]. We extracted the anharmonic IFCs up to the fourth order and kept all the harmonic IFCs within the $3 \times 3 \times 3$ supercell. Cutoff radii of 6.35 and 4.23 Å were adopted to obtain the cubic and quartic IFCs, respectively.

The SCP calculations [17,18] at finite temperatures were performed to obtain the anharmonic phonon frequencies and eigenvectors using the extracted 0 K harmonic and anharmonic IFCs. The temperature-dependent anharmonic frequencies $\Omega_{\boldsymbol{q}j}(T)$ and polarization vectors $\varepsilon_{\boldsymbol{q}j}(T)$ were obtained by diagonalizing the following matrix $V_{\boldsymbol{q}}$ defined as [15,17]

$$V_{\boldsymbol{q}jj'} = \omega_{\boldsymbol{q}j}^2 \delta_{jj'} + \frac{1}{2} \sum_{q'} \Phi(\boldsymbol{q}j; -\boldsymbol{q}j'; q'; -q') \langle Q_{q'}^* Q_{q'} \rangle, \quad (1)$$

$$\langle Q_{q'}^* Q_{q'} \rangle = \left[\frac{\hbar}{2\Omega_{q'}} \right] [1 + 2n(\Omega_{q'})]. \quad (2)$$

Here, $\omega_{\boldsymbol{q}j}$ is the harmonic phonon frequency associated with the wave vector $\boldsymbol{q}$ and phonon branch j. Also, $\langle Q_{q'}^* Q_{q'} \rangle$ is the mean squared displacement (MSD) of the normal coordinate Q. Here, the q in the expression is the shorthand notation for a composite index of the wave vector and phonon branch $(\boldsymbol{q}, j)$ and satisfying $q = (\boldsymbol{q}, j)$ and $-q = (-\boldsymbol{q}, j)$. Further, $\Phi(\boldsymbol{q}j; \boldsymbol{q}j'; q'; -q')$ is the reciprocal representation of fourth-order IFCs, and $n(\omega) = 1/[\exp(\hbar\omega/k_B T) - 1]$ is the

Bose-Einstein distribution (k_B is the Boltzmann constant, and $\hbar$ is the reduced Planck constant).

We also considered the off-diagonal components of the self-energy to allow for polarization mixing (PM), which we found to be important for the $BaZrO_3$ system, particularly at the Γ-symmetry point in the Brillouin zone [see Figs. S2(a) and S2(b) in the Supplemental Material (SM) [39] (see also Refs. [40–42] therein)]. If we neglected the off-diagonal elements, the SCP equation can be reduced to the following diagonal form:

$$\Omega_q^2 = \omega_q^2 + 2\Omega_q I_q, \tag{3}$$

$$I_q = \frac{1}{2}\sum_{q'} \frac{\hbar\Phi(q;-q;q';-q')}{4\Omega_q\Omega_{q'}}[1+2n(\Omega_{q'})]. \tag{4}$$

In this study, the $\boldsymbol{q}$ mesh of the SCP calculations was set to $3\times3\times3$, and the inner $\boldsymbol{q}'$ was set to $9\times9\times9$ to achieve convergence of anharmonic phonon frequencies.

To this end, the anharmonic phonon renormalization only considers the loop diagram ascribing from the quartic IFCs, namely, the first-order SCP calculations. However, phonon frequency shifts induced by the cubic anharmonicity (the cubic IFCs) may not be negligible [16,19]. The frequency shifts due to the bubble diagram were found to be negative and contributed to resolving the overestimation in phonon hardening from the quartic anharmonicity. Meanwhile, we also carefully examined the tadpole diagram calculated by the cubic IFCs, and it is negligible. Instead of employing a perturbative manner [43], on top of the first-order SCP calculations, additional negative frequency shifts resulting from the bubble self-energy were estimated within quasiparticle approximation using the following self-consistent equation [19]:

$$\Omega_{q,\mathrm{B}}^2 = \Omega_q^2 - 2\Omega_q \mathrm{Re}\sum_q^{\mathrm{B}}(\Omega_q), \tag{5}$$

$$\sum_q^{\mathrm{B}}(\Omega_q) = \frac{1}{2\hbar^2}\sum_{q_1,q_2,s=\pm1}|V_3(-q;q_1;q_2)|^2 \times\left[\frac{(n_1+n_2+1)}{s\Omega_c+\Omega_{q_1}+\Omega_{q_2}} - \frac{n_1-n_2}{s\Omega_c+\Omega_{q_1}-\Omega_{q_2}}\right]. \tag{6}$$

Here, $\sum_q^B(\Omega_q)$ is the phonon frequency-dependent bubble self-energy, $\Omega_c = \Omega_q + i0^+$, with 0^+ being a positive infinitesimal, B denotes bubble diagram, and V_3 is the 3ph interaction strength [17,43]. In this paper, the IFC estimations and SCP calculations were performed by using the ALAMODE package [17,44].

We next introduce the equations of thermodynamics and lattice thermal conductivity κ_L considering the effect of the cubic and quartic lattice anharmonicities. These equations are identical to those commonly used in the thermal conductivity calculations except that harmonic phonon frequencies and eigenvectors are substituted by anharmonically renormalized frequencies and eigenvectors obtained by the SCP calculations, respectively. Based on the obtained harmonic (both the original and renormalized second-order force constants) and anharmonic IFCs, i.e., third- and fourth-order IFCs, the lattice thermal conductivity κ_L can be calculated by solving the Peierls-Boltzmann transport equation (PBTE). The linearized PBTE can be written as [45,46]

$$\boldsymbol{F}_q = \tau_q^0(\boldsymbol{v}_q + \Delta_q), \tag{7}$$

where τ_q^0 denotes the phonon relaxation time of mode q within single-mode relaxation time approximation (SMRTA), $\boldsymbol{v}_q$ denotes the intraband phonon group velocity corresponding to mode q, and Δ_q represents a correction term denoting the phonon population deviation from the SMRTA scheme. The detailed form of Δ_q including 3ph, 4ph, and isotope-phonon scattering terms can be expressed as

$$\begin{aligned}\Delta_\lambda = {}& \frac{1}{N_0}\sum_{q'q''}^{(+)}\Gamma^{(+)}_{qq'q''}(\xi_{qq''}F_{q''} - \xi_{qq'}F_{q'}) \\ & + \frac{1}{N_0}\sum_{q'q''}^{\bar{}}\frac{1}{2}\Gamma^{(-)}_{qq'q''}(\xi_{qq''}F_{q''} + \xi_{qq'}F_{q'}) \\ & + \frac{1}{N_0}\sum_{q'q''q'''}^{(++)}\frac{1}{2}\Gamma^{(++)}_{qq'q''q'''}(\xi_{qq'''}F_{q'''} - \xi_{qq'}F_{q'} - \xi_{qq''}F_{q''}) \\ & \times\frac{1}{N_0}\sum_{q'q''q'''}^{(+-)}\frac{1}{2}\Gamma^{(+-)}_{qq'q''q'''}(\xi_{qq'''}F_{q'''} - \xi_{qq'}F_{q'} + \xi_{qq''}F_{q''}) \\ & \times\frac{1}{N_0}\sum_{q'q''q'''}^{(--)}\frac{1}{6}\Gamma^{(--)}_{qq'q''q'''}(\xi_{qq'''}F_{q'''} + \xi_{qq'}F_{q'} + \xi_{qq''}F_{q''}) \\ & + \frac{1}{N_0}\sum_{q'}^{(\mathrm{iso})}\Gamma^{(\mathrm{iso})}_{qq'}\xi_{qq'}F_{q'},\end{aligned} \tag{8}$$

and using Matthiessen's rule, the phonon relaxation time τ_q^0 can be expressed as

$$\begin{aligned}\frac{1}{\tau_q^0} = {}& \frac{1}{N_0}\left[\sum_{q'q''}^{(+)}\Gamma^{(+)}_{qq'q''} + \sum_{q'q''}^{(-)}\frac{1}{2}\Gamma^{(-)}_{qq'q''}\right] + \frac{1}{N_0}\sum_{q'}^{(\mathrm{iso})}\Gamma^{(\mathrm{iso})}_{qq'} \\ & + \frac{1}{N_0}\left[\sum_{q'q''q'''}^{(++)}\frac{1}{2}\Gamma^{(++)}_{qq'q''q'''} + \sum_{q'q''q'''}^{(+-)}\frac{1}{2}\Gamma^{(+-)}_{qq'q''q'''}\right. \\ & \left. + \sum_{q'q''q'''}^{(--)}\frac{1}{6}\Gamma^{(--)}_{qq'q''q'''}\right],\end{aligned} \tag{9}$$

where the shorthand notation $\xi_{qq'} = \omega_{q'}/\omega_q$, N_0 represents the total number of sampled phonon wave vectors in the first Brillouin zone, the superscripts $(+-)$ or $(++,+-,--)$ denote the 3ph and 4ph scattering processes, i.e., $\boldsymbol{q}'' = \boldsymbol{q}\pm\boldsymbol{q}'+\boldsymbol{Q}$ and $\boldsymbol{q}''' = \boldsymbol{q}\pm\boldsymbol{q}'\pm\boldsymbol{q}''+\boldsymbol{Q}$, respectively, where $\boldsymbol{Q}$ is a reciprocal-lattice vector, and 3ph and 4ph scattering rates Γ in Eqs. (8) and (9) take the form of

$$\Gamma^{(\pm)}_{qq'q''} = \frac{\hbar\pi}{4}\frac{\left\{\begin{matrix} n_{q'}-n_{q''} \\ n_{q'}+n_{q''}+1\end{matrix}\right\}}{\omega_q\omega_{q'}\omega_{q''}}|V^{(\pm)}_{qq'q''}|^2\delta(\omega_q\pm\omega_{q'}-\omega_{q''}), \tag{10}$$

$$\Gamma^{\left(\begin{smallmatrix}++\\+-\\--\end{smallmatrix}\right)}_{qq'q''q'''} = \frac{\hbar^2\pi}{8N_0}\frac{\left\{\begin{smallmatrix}(1+n_{q'})(1+n_{q''})n_{\lambda'''}\\(1+n_{q'})n_{q''}n_{q'''}\\n_{q'}n_{q''}n_{q'''}\end{smallmatrix}\right\}}{n_q} \times \left|V^{\left(\begin{smallmatrix}++\\+-\\--\end{smallmatrix}\right)}_{qq'q''q'''}\right|^2 \frac{\delta\left(\omega_q\begin{bmatrix}+\\+\\-\end{bmatrix}\omega_{q'}\begin{bmatrix}+\\-\\-\end{bmatrix}\omega_{q''}-\omega_{q'''}\right)}{\omega_q\omega_{q'}\omega_{q''}\omega_{q'''}}, \tag{11}$$

where $V_{qq'q''}$ and $V_{qq'q''q'''}$ denote the 3ph and 4ph scattering matrix elements, respectively [47]. Using the determined $\boldsymbol{F}_q$ by solving Eq. (7) iteratively, the phonon tensor-dependent thermal conductivity κ_{L} can be obtained as

$$\kappa_{\mathrm{L}}^{\alpha\beta} = \frac{\hbar^2}{k_{\mathrm{B}}T^2VN_0}\sum_q n_q(n_q+1)(\hbar\omega_q)^2\upsilon_q^\alpha F_q^\beta, \tag{12}$$

where T is the temperature, V is the unit-cell volume, and υ is the phonon group velocity. Within the SMRTA scheme, Eq. (12) can be expressed as $\kappa_{\mathrm{L}}^{\alpha\beta} = (1/VN_0)\sum_q c_q\upsilon_q^\alpha\upsilon_q^\beta\tau_q^0$ with the phonon mode-specific heat c_q. Note that the iterative scheme to PBTE is only applied for 3ph scattering processes in this paper, while the 4ph scattering processes are treated at the SMRTA level considering the exceptionally large memory demands [47].

Conventionally, the Peierls-Boltzmann transport theory neglects the coherence terms, i.e., off-diagonal terms of the heat flux operators, which is valid when the phonon interbranch spacings are much larger than the linewidths [23,48]. However, when the phonon mean free path (MFP) approaches the interatomic spacing, the off-diagonal contributions become nonnegligible and can be calculated by a unified theory of thermal transport. The resulting formula for κ_{L} within the SMRTA is given as follows [23]:

$$\kappa_{\mathrm{L}}^{\mathrm{P/C}} = \frac{\hbar^2}{k_{\mathrm{B}}T^2VN_0}\sum_{\boldsymbol{q}}\sum_{j,j'}\frac{\omega_{\boldsymbol{q}j}+\omega_{\boldsymbol{q}j'}}{2}\boldsymbol{\upsilon}_{\boldsymbol{q}jj'}\otimes\boldsymbol{\upsilon}_{\boldsymbol{q}j'j} \times \frac{\omega_{\boldsymbol{q}j}n_{\boldsymbol{q}j}(n_{\boldsymbol{q}j}+1)+\omega_{\boldsymbol{q}j'}n_{\boldsymbol{q}j'}(n_{\boldsymbol{q}j'}+1)}{4(\omega_{\boldsymbol{q}j}-\omega_{\boldsymbol{q}j'})^2+(\Gamma_{\boldsymbol{q}j}+\Gamma_{\boldsymbol{q}j'})^2}(\Gamma_{\boldsymbol{q}j}+\Gamma_{\boldsymbol{q}j'}), \tag{13}$$

where the superscripts P and C represent the propagation and coherence contributions, respectively. Here, $\Gamma_{\boldsymbol{q}j}$ represents the scattering rates including isotope-phonon, 3ph, and 4ph scattering processes. The interbranch generalization of group velocity is given as [49]

$$\boldsymbol{\upsilon}_{\boldsymbol{q}j'j} = \frac{\langle e_{\boldsymbol{q}j}|\frac{\partial D(\boldsymbol{q})}{\partial\boldsymbol{q}}|e_{\boldsymbol{q}j'}\rangle}{2\sqrt{\omega_{\boldsymbol{q}j}\omega_{\boldsymbol{q}j'}}}, \tag{14}$$

where $D(\boldsymbol{q})$ is the dynamical matrix, and $e_{\boldsymbol{q}j}$ is the polarization vector. The phonon band diagonal term ($j=j'$) corresponds to Peierls's contribution (population contribution; $\kappa_{\mathrm{L}}^{\mathrm{P}}$) and the off-diagonal terms ($j\neq j'$) give the coherence contribution ($\kappa_{\mathrm{L}}^{\mathrm{c}}$), and their summation gives the total lattice thermal conductivity $\kappa_{\mathrm{L}} = \kappa_{\mathrm{L}}^{\mathrm{P}} + \kappa_{\mathrm{L}}^{\mathrm{C}}$. In this paper, the $\boldsymbol{q}$ mesh of the PBTE for 3ph scattering processes was set to $14\times14\times14$, which gives well-converged results for the cubic $BaZrO_3$ system [17]. Considering the huge computational cost, a $\boldsymbol{q}$ mesh of $12\times12\times12$ with a scalebroad parameter of 0.06 was used for 4ph scattering processes to solve the PBTE. Thermal transport calculations including phonon and coherent thermal transport channels were performed by using the SHENGBTE and FOURPHONON packages [47,50].

III. RESULTS AND DISCUSSION

A. Lattice dynamics

Lattice anharmonicity ascribing from the cubic and quartic IFCs determines the reliable modeling of lattice dynamics. We first investigated the impact of lattice anharmonicity on phonon dispersions in cubic $BaZrO_3$ crystal [see Fig. 1(a)]. The calculated phonon dispersions with different levels of theory (HA and SCP calculations) are shown in Fig. 1(d). Correspondingly, the temperature-dependent bond strengths (calculated by the second-order IFCs) renormalized by lattice anharmonicity are plotted in Figs. S1(a)–S1(f) in the SM [39], which shows that the self-interaction strengths of all atoms and the nearest-neighbor bond strengths of Zr-O and O-O increase with increasing temperature, while other bonds become softer. As expected, the HA phonon dispersions do not exhibit imaginary frequencies in the whole Brillouin zone, indicating the dynamical stability at 0 K for cubic crystalline $BaZrO_3$, in agreement with the experimental observation [32]. As the temperature increases, continuous phonon hardening happens, evident for low-frequency optical phonon modes (<6 THz) at the Γ-(0.0,0.0,0.0), M-(0.5,0.5,0.0), and R- (0.5,0.5,0.5) high-symmetry points. Such phonon hardening of optical modes has been experimentally observed in crystalline $BaZrO_3$ and its analogs [25,26,51]. This phenomenon is unusual, as most materials show phonon softening at higher temperatures due to weaker bonding strengths.

The low-frequency optical modes at Γ, M, and R points are identified to be the ferroelectric (Γ_{15}) mode and in-phase and out-of-phase antiferroelectric distortive (AFD; M_3 and R_{25}) modes, which are associated with atomic antiparalleled motions in the unit cell and in-phase and out-of-phase tilts of ZrO_6 octahedra, respectively. Figure 1(d) also shows the atom-decomposed partial and total phonon density of states (DOS), indicating that acoustic phonon modes are mainly contributed by the vibrations of Ba atoms (giving rise to a sharp DOS peak centered at ∼2.4 THz), while the optical modes are dominated by O and Zr atoms. These features are also clearly reflected by the atomic participation ratio of all atoms projected onto the phonon dispersions, as presented in Figs. S3(a)–S3(c) in the SM [39].

Compared with the notable phonon hardening of low-frequency optical modes, the acoustic phonon modes (largely contributed by the Ba vibrations) become only slightly harder, and the intermediate-frequency optical modes (dominated by Zr atoms) undergo negligible hardening with increasing temperature, as depicted in Figs. 1(d) and S3(a)–S3(c) in the SM [39]. In contrast, most high-frequency optical modes (between 10 and 15 THz) with the majority contribution from O atoms become softer with the increasing

temperature, which is consistent with the experimental observations [see the transverse optical (TO) mode (Axe) in Fig. 1(c)] [52,53]. It is worth noting that both the cubic and quartic IFCs are important for reproducing accurate dispersions for this strongly anharmonic material. Only considering the quartic IFCs tends to overestimate phonon frequency [16,19] due to the neglection of the negative phonon frequency shifts caused by bubble self-energy (the cubic IFCs), failing at producing the phonon softening in the high-frequency modes within 10–15 THz at finite temperatures (see Figs. S2(a) and S2(b) in the SM [39]) [19]. To illustrate it, we calculated the squared phonon frequency of the R_{25} mode as a function of temperature using different methods, i.e., the first-order SCP calculations with polarization mixing (PM) and that with the bubble diagram further included, as shown in Fig. 1(b). Indeed, Fig. 1(b) shows that the anharmonic phonon renormalization incorporating the bubble diagram significantly suppresses the phonon frequency compared with the first-order SCP calculations with PM as temperature increases. Compared with the experimental results by Perrichon *et al.* [33], we predict a relatively stronger temperature dependence of the frequency of the R_{25} mode. A detailed discussion about this discrepancy is provided in the SM (see Fig. S4 and the corresponding discussion) [39]. Nevertheless, the anharmonic phonon renormalization considering bubble self-energy correction accurately reproduces the phonon softening in the high-frequency optical modes (between 10 and 15 THz at the Γ point) with increasing temperature [see Fig. 1(d)], in line with the experimental observation [52,53]. The predicted phonon softening ascribes to the results of competition between the phonon hardening from the loop diagram (the quartic anharmonicity) and phonon softening from the bubble diagram (the cubic anharmonicity). However, both the first-order SCP calculations (with/without PM) fail to produce the experimentally observed phonon softening, as reported in Figs. S2(a) and S2(b) in the SM [39], highlighting the necessity of considering the bubble self-energy correction in anharmonic phonon renormalization for $BaZrO_3$. Here, we need to emphasize that all the frequency shifts induced by bubble and loop diagrams were estimated using the nonperturbative manner, i.e., the SCP method, in this paper. This is because the frequency shifts of low-frequency optical modes are comparable with their frequencies with increasing temperature, e.g., the R_{25} mode, which results in the invalidity of perturbative manner [43]. The frequency shifts of the R_{25} mode calculated by the perturbative and nonperturbative methods are presented in Fig. S5 in the SM [39], respectively; indeed, the large difference in frequency shift exhibits between the perturbative and nonperturbative methods. To verify our calculation, we compare the calculated optical phonon frequencies and experimental values [52] at finite temperatures, in Fig. 1(c), observing good agreement between them and clearly illustrating the phonon hardening of low-frequency optical modes [TO1(Last) and TO2(Slater)] and softening of high-frequency modes [TO(Axe)]. In contrast, the conventional HA method cannot capture these temperature-induced frequency shifts.

To understand the phonon-hardening-induced-by-temperature effect, we calculated the PESs of the lowest optical TO1 (Γ_{15}) and in-phase (M_3) and out-of-phase tilting modes (R_{25}) by displacing atoms by $\mu_k = M_\kappa^{1/2} e_{q,k}\eta$, where M_k, $e_{q,\kappa}$, and η are the atomic mass of atom κ, eigenvector of atom κ at the q point, and the amplitude of the normal mode coordinate, respectively, as shown in Figs. 2(a)–2(c). All the PESs of these low-frequency optical modes show the presence of a relatively deep energy well with a flat bottom. The U-shaped PESs remarkably deviate from the HA (second-order fitting) [see Figs. 2(a)–2(c)] when atomic collective motions are in large magnitude at elevated temperatures. Indeed, the O atoms exhibit large mean squared atomic displacements at elevated temperatures [see Fig. 2(d)]. The U-shaped PESs of those optical modes can be approximated by a fourth-order polynomial [54] [solid blue lines in Figs. 2(a)–2(c)], indicating strong quartic anharmonicity at high temperatures. Therefore, the phonon hardening in crystalline $BaZrO_3$ stems from the lattice anharmonicity-induced phonon renormalization. Moreover, a close inspection further reveals that Γ_{15}, M_3, and R_{25} modes have a majority contribution from the Zr-O bonds, of which the nearest-neighbor second-order IFCs are enhanced significantly (see Fig. S1(e) in the SM [39]).

We then examined the effect of phonon hardening on lattice thermodynamic properties, including MSDs, phonon intraband group velocity, and phonon specific heat [see Figs. 2(d)–2(f)]. The O atoms possess the largest MSD compared with the other two elements [see Fig. 2(d)], consistent with the experimental observations [33]. The MSD by the HA is often overestimated, while the anharmonic phonons further suppress the MSD of all the atoms, thereby producing better agreement with experimental results. Specifically, the MSD of the atom O_{11} calculated by the SCP method agrees quite well with the experimental values at $T = 300$ K [33] [see inset in Fig. 2(d)]. This observation in MSD manifests the significance of accurate treatment of lattice anharmonicity in lattice dynamics modeling. In contrast, the SCP and HA methods produce indistinguishable results for the phonon specific heat [see Fig. 2(e)], which reasonably agree with the experimental results [9,56]. Meanwhile, the phonon mode group velocities decrease slightly within the frequency range of 1–4 THz with increasing temperature, as shown in Fig. 2(f). This is because the anharmonic phonon renormalization flattens the optical phonon branches in the corresponding frequency region [see Fig. 1(d)].

B. Lattice thermal conductivity

We next investigate the effect of lattice anharmonicity-induced anharmonic phonon renormalization on the lattice thermal conductivity κ_L in crystalline $BaZrO_3$. The κ_L was calculated within different levels of thermal transport theory, namely, the HA/SCP+3/3,4ph and HA/SCP+3,4ph+OD models, as presented in Fig. 3(a). In the particlelike phonon picture, Peierls' lattice thermal conductivity κ_L^P was calculated by the PBTE [21]. The lattice thermal conductivities κ_L^P obtained from the lowest level of thermal transport theory, namely, the HA+3ph model, are 5.93 and 1.24 $Wm^{-1}K^{-1}$ at 300 and 1500 K, respectively [see Fig. 3(a)]. As highlighted in the previous section, anharmonic phonon renormalization plays a crucial role in accurately predicting finite-temperature phonon energies. Hence, we improve the HA+3ph model to a more accurate model, i.e., the SCP+3ph model, by

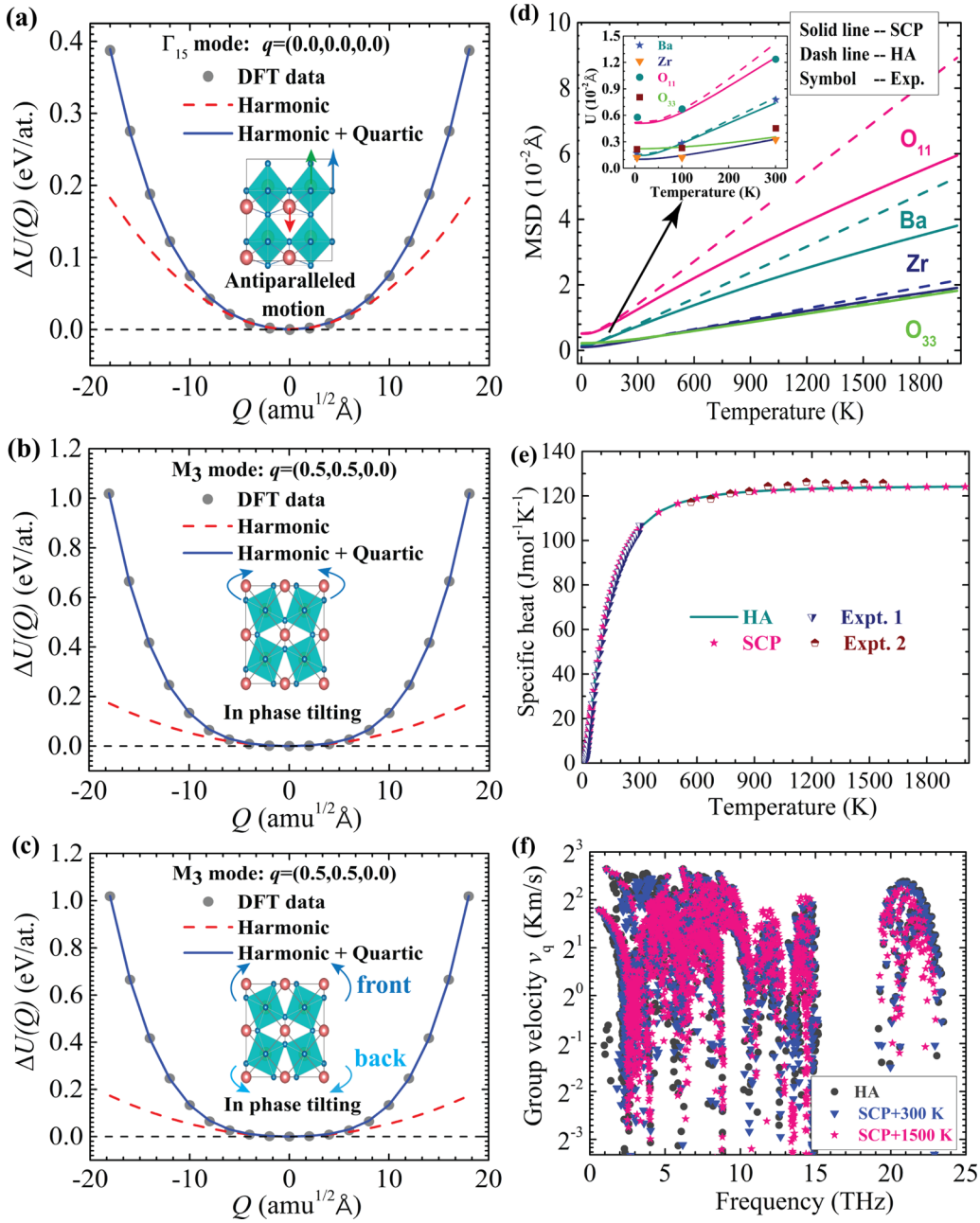

FIG. 2. (a) Calculated potential energy surface (PES) of the lowest optical phonon mode (TO1, Γ_{15}) at the Γ point. (b) PES of the in-phase tilting mode (M_3) at the M point. (c) PES of the out-of-phase tilting mode (R_{25}) at the R point. (d) Calculated mean squared displacements (MSDs) as a function of temperature. The dashed and solid lines correspond to the results obtained by harmonic approximation (HA) and self-consistent phonon (SCP) calculations, respectively. Inset: Calculated MSDs in comparison with those observed in experiments [33]. The atomic MSD is a tensor-dependent variable [55], and 1 and 3 denote the Cartesian coordinates x and z, respectively. (e) Calculated mode-specific heat with SCP calculation as a function of temperature in comparison with experimental results [9,56] and those from HA calculations. (f) Calculated anharmonic phonon group velocities at $T = 300$ and 1500 K in comparison with those from the HA calculation at $T = 0$ K.

considering phonon frequency shifts. Figure 3(a) shows that the effects of anharmonic phonon renormalization on κ_L^P are quite significant, and the corresponding calculated κ_L^P has values of 8.31 and 2.64 $Wm^{-1}K^{-1}$ at 300 and 1500 K, respectively. Similarly, a significant enhancement in κ_L^P calculated using the SCP+3ph model were observed over the entire temperature range (300–2000 K) compared with those predicted by the HA+3ph model. This reveals that the anharmonic phonon renormalization from the cubic and quartic anharmonicities indeed plays a critical role in enhancing phonon thermal transport at the lowest perturbation theory level, i.e., considering only the 3ph scattering processes. However, it is worthwhile mentioning here that the quartic anharmonicity not only induces large phonon frequency shifts but also brings about strong 4ph scatterings. With further including additional 4ph scatterings, Fig. 3(a) shows that κ_L^P

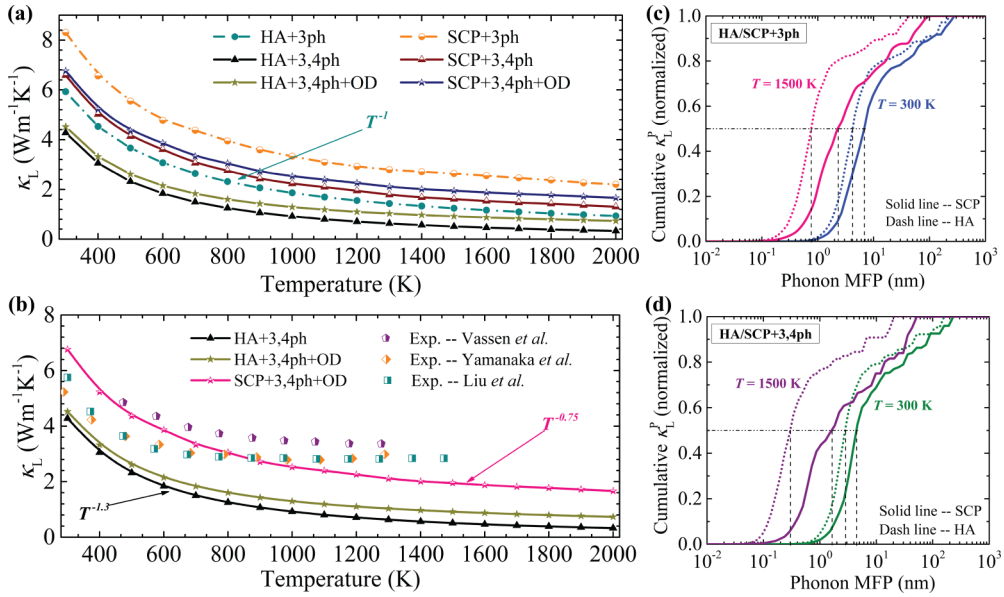

FIG. 3. (a) Calculated temperature-dependent lattice thermal conductivity κ_L based on different levels of thermal transport theory including the harmonic approximation (HA)/self-consistent phonon (SCP)+3/3,4ph, HA/SCP+3,4ph+OD models. (b) Calculated thermal conductivity κ_L using the HA+3,4ph and HA/SCP+3,4ph+OD models compared with the experimental results [9,11,12]. (c) Calculated cumulative phonon thermal conductivity as a function of phonon mean free path within the HA/SCP+3ph models at $T = 300$ and 1500 K, respectively. (d) The same as (c) but within the HA/SCP+3,4ph models.

calculated with HA/SCP+3,4ph relative to HA/SCP+3ph models decreased by 27.84/20.78 and 59.00/38.85% at 300 and 1500 K, respectively. Interestingly, considering anharmonic phonon renormalization dramatically suppresses the effect of 4ph scattering processes on thermal transport in $BaZrO_3$. In addition, the anharmonic phonon renormalization and 4ph scattering processes induced by quartic anharmonicity have the opposite effect on thermal transport. Therefore, compared with κ_L^P computed using the HA+3ph model, the enhancement in κ_L^P is the outcome of the competition between the phonon hardening and 4ph scattering induced by the quartic anharmonicity.

We continue to examine the frequency-dependent MFPs at 300 and 1500 K, respectively, as shown in Figs. S6(a)–S6(d) in the SM [39]. For all the HA/SCP+3/3,4ph calculations, many phonon modes possess MFPs close to or lower than the minimum interatomic distances at 1500 K, despite the anharmonic phonon renormalization increases the phonon MFPs, indicating the necessity of considering coherence contributions at elevated temperatures. To evaluate the effect of coherence contributions on thermal transport in $BaZrO_3$, we next move up the theory level to the HA/SCP+3,4ph+OD models which consider phonon and coherence contributions from both the cubic and quartic anharmonicity [see Fig. 3(a)]. The main findings in thermal transport computed with the HA/SCP+3,4ph+OD models are as follows: (i) Additional off-diagonal terms of the heat flux operators calculated by the cubic and quartic anharmonicity enhance thermal transport over the entire temperature range, particularly at high temperatures, e.g., at 1500 K. (ii) Further including 4ph scattering makes the coherence contribution more important, even changing the microscopic mechanism of thermal transport (coherence contribution dominates heat conduction) at extremely high temperatures, e.g., 2000 K, based on the HA+3,4ph+OD model [see Fig. 3(a) and later analysis of Fig. 6(a)]. (iii) Compared with the coherence contribution, the anharmonic phonon renormalization plays a dominant role in enhancing κ_L in crystalline $BaZrO_3$. (iv) Finally, 4ph scattering significantly suppresses the phonon transport, whereas κ_L calculated using the highest level of thermal transport theory in this paper, namely, the SCP+3,4ph+OD model, is still larger than that predicted by the HA+3ph model. This highlights the critical role of anharmonic phonon renormalization in enhancing the total κ_L.

To verify the validity of the highest level of thermal transport theory in this paper, namely, the SCP+3,4ph+OD model, in predicting thermal transport in crystalline $BaZrO_3$, we compared κ_L computed by HA+3,4ph and HA/SCP+3,4ph+OD models with those obtained from experiments [9,11,12]. As shown in Fig. 3(b), the predicted κ_L^P by the HA+3,4ph model of $BaZrO_3$ is ~25.64–82.03% lower than the experimental results from Liu *et al.* [11] and Yamanaka *et al.* [12] from 300 to 1500 K. The predicted κ_L by the HA+3,4ph+OD model are also significantly lower than the measured κ_L from Vassen *et al.* [9]. This reveals the invalidity of the conventional HA method in modeling phonon thermal transport in $BaZrO_3$ due to its strong anharmonicity. Further including anharmonic phonon renormalization induced by cubic and quartic anharmonicities, namely, the SCP+3,4ph+OD model, significantly improves the agreement between the predicted κ_L and experimental values over a wide temperature range [9,11,12] [see Fig. 3(b)]. This highlights the importance of proper treatment of anharmonic phonon renormalization in modeling simple but highly anharmonic crystals. However, the discrepancies between the measured and predicted κ_L using the SCP+3,4ph+OD model are still observed at high temperatures in Fig. 3(b), which may be attributed to the following reasons: (i) contribution of electronic thermal

conductivity at high temperatures; (ii) lack of high-order terms of the heat flux operators, namely, the anharmonic contributions of the heat flux operators, which may have an important contribution to the total κ_L at high temperatures [57]; and (iii) thermal radiation heat loss during the measurement at elevated temperatures. Although the SCP+3,4ph+OD model does not accurately reproduce the experimental κ_L over the entire temperature range, it reveals the importance of proper treatment of lattice anharmonicity and coherent thermal transport channel in predicting κ_L for highly anharmonic materials.

We next proceed to examine the effect of anharmonic phonon renormalization and high-order phonon scattering process on the temperature dependence of lattice thermal conductivity κ_L. As expected, the predicted Peierls' thermal conductivity κ_L^P considering only the 3ph scattering process and using 0 K second-order force constants, i.e., obtained by the HA+3ph model, follows temperature dependence of $\kappa_L \sim T^{-1}$ [see Fig. 3(a)]. The additional 4ph scattering effect (HA+3,4ph model) not only significantly suppresses κ_L^P but also drastically changes the temperature dependence of thermal conductivity to $T^{-1.3}$, which shows a strong temperature dependence and is consistent with the observations from Feng *et al.* [58] (note that, to compare with the experiments, we only do the first-order fitting to the temperature dependence of thermal conductivity, although Feng *et al.* [58] proposed a second-order fitting for the temperature dependence of κ_L when further considering 4ph scatterings. In general, further considering 4ph scatterings results in stronger temperature dependence of the κ_L than that calculated by the lowest perturbation theory). Further considering anharmonic phonon renormalization and coherence contributions results in the weaker temperature dependence of $T^{-0.75}$, which explains the experimental weak temperature dependence of κ_L [see Fig. 3(b)]. This highlights again that the anharmonic phonon renormalization plays a determining role in reproducing the magnitude of the experimental κ_L and its temperature-dependence relation in ternary perovskite-type oxides, e.g., $BaZrO_3$.

To this end, we start to analyze the phonon propagation and coherence channels individually due to their different mechanisms of thermal transport. We calculated the cumulative κ_L^P as a function of the MFP at 300 and 1500 K using the HA/SCP+3/3,4ph models, respectively, as presented in Figs. 3(c) and 3(d). The thermal conductivity calculated by the HA/SCP+3/3,4ph models is almost saturated when the MFP is >200 nm at both temperatures. The MFPs corresponding to 50% thermal conductivity accumulation based on the SCP+3ph(SCP+3,4ph) models are 7(4.4) and 2.3(1.6) nm at 300 and 1500 K, respectively. This suggests that the thermal transport in $BaZrO_3$ is dominated by the short-MFP phonons, indicating strong anharmonic phonon scattering in crystalline $BaZrO_3$. The short MFPs rationalize the weak size effects of thermal conductivity for $BaZrO_3$. When the HA+3/3,4ph models were used, the calculated cumulative κ_L^P curves significantly shift to the left side, especially at 1500 K.

To gain insight into the microscopic mechanisms of phonon thermal transport in crystalline $BaZrO_3$, we calculated the cumulative κ_L^P and spectral $\kappa_L^P(\omega)$ based on the HA/SCP+3/3,4ph models at 300 and 1500 K, respectively, as presented in Figs. 4(a) and 4(b). Here, κ_L^P is mainly contributed by the phonon modes with a frequency <10 THz. The contributions to κ_L^P from acoustic modes based on all the theoretical models are $\lesssim 50\%$ over the temperature range from 300 to 1500 K [see Figs. 4(c) and 4(d)], indicating that the optical modes dominate heat conduction in $BaZrO_3$. Similar behavior is also observed in the same family of perovskite oxide $SrTiO_3$ [17]. Specifically, the lowest TO1 branches contribute ~10% of the total κ_L^P at different temperatures with the HA/SCP+3/3,4ph models due to its dispersive phonon branch [see Figs. 1(d), 4(c), and 4(d)]. Also, the relative thermal conductivity contributions from acoustic modes are enhanced due to the reduced coupling between acoustic and optical phonons induced by the anharmonic phonon renormalization [see Figs. 4(c) and 4(d)]. Our subsequent analysis will show that the contribution to the total κ_L^P from acoustic modes is strongly suppressed because of its strong coupling with the low-frequency optical phonons. In addition, with additional 4ph scatterings, the relative κ_L^P contributions from acoustic modes calculated with SCP+3,4ph relative to the SCP+3ph model are also enhanced. This can be attributed to the low-optical phonon hardening and the large 4ph scattering rates existing in the low-frequency optical phonon region, resulting in the enhancement and suppression in κ_L^P contributed from the acoustic and optical modes, respectively [see Figs. 4(e) and 4(f)].

Again, the anharmonic phonon renormalization significantly enhances the thermal transport calculated using the SCP+3/3,4ph models at 300 and 1500 K, respectively, and the enhancement in κ_L^P is more obvious by further including the 4ph scattering processes [see Figs. 4(a) and 4(b)]. We next explore the origin of the enhancements in κ_L^P, as presented in Figs. 4(a) and 4(b); the enhancement in κ_L^P calculated by the SCP+3/3,4ph models at both 300 and 1500 K mainly comes from the phonon modes <6 THz. Specifically, the overall relative enhancement in κ_L^P computed by the SCP+3/3,4ph models sees an increase, percentagewise, from 40.15/53.86% at 300 K to 111.90/216.08% at 1500 K. Compared with optical modes, acoustic modes contribute more to the relative enhancement in κ_L^P considering the 4ph process, specifically, 29.25 and 127.85% increase at 300 and 1500 K, respectively. However, considering only the 3ph process, the acoustic and optical modes play an equal role in enhancing κ_L^P [see Figs. 4(a)–4(d)]. This highlights the importance of the 4ph scattering process in accurately describing thermal transport in cubic perovskite $BaZrO_3$ and reveals that the renormalized acoustic modes dominate the enhancements in computed κ_L^P, although the optical modes dominate the heat conduction.

According to the kinetic theory, the changes in specific heat induced by lattice anharmonicity are negligible, and the phonon group velocities show a slight decrease within 1–4 THz [see Figs. 2(e) and 2(f)], the enhancement in κ_L^P is therefore attributed to the suppression in 3ph and 4ph scattering rates by the anharmonic phonon renormalization. Indeed, the comparison of the phonon scattering rates calculated by the HA+3/4ph and SCP+3/4ph models in Figs. 4(e), 4(f), S7(a), and S7(b) in the SM [39], shows a reduction in 3ph and 4ph scattering rates of those phonon modes lying <6 THz, evident for the 4ph scattering process and at 1500 K, in line

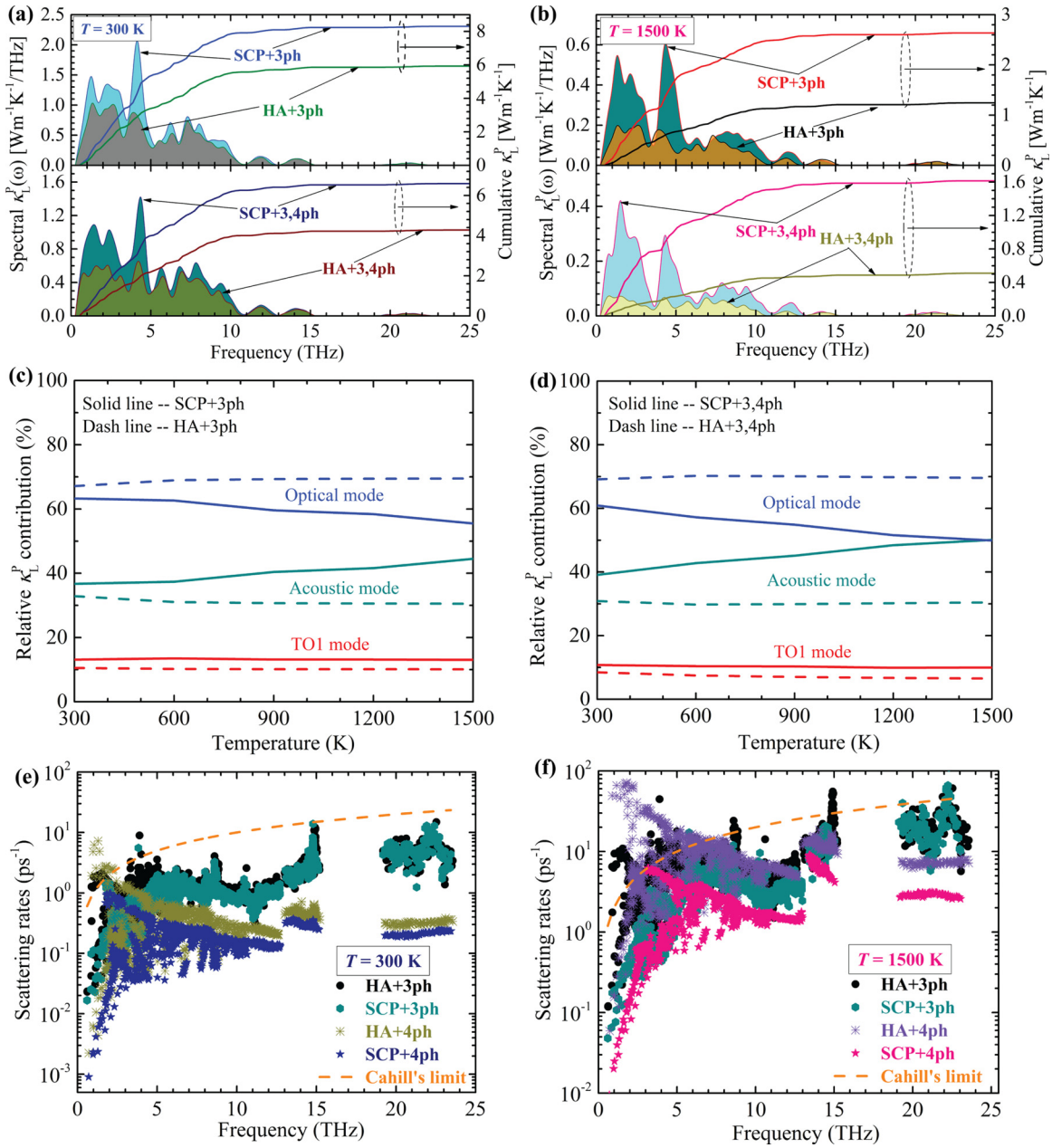

FIG. 4. Comparison between the harmonic approximation (HA)+3/3,4ph and self-consistent phonon (SCP)+3/3,4ph models. (a) Spectral and cumulative lattice thermal conductivities at $T = 300$ K. (b) The same as (a) but $T = 1500$ K. (c) Thermal conductivity contributions from the total acoustic, optical, and the lowest TO1 branches calculated using the HA/SCP+3ph models, respectively. (d) The same as (c) but using the HA/SCP+3,4ph models. (e) Calculated three- and four-phonon scattering rates using the harmonic and anharmonic frequencies and eigenvectors at $T = 300$ K, respectively. (f) The same as (e) but $T = 1500$ K. The dash yellow line assumes the scattering rate to be twice the phonon frequency to estimate minimum κ_L [59], and the phonons are well-defined when their scattering rates are below this line.

with the enhancement in the spectral $\kappa_L^P(\omega)$ in Figs. 4(a) and 4(b). Moreover, the anharmonic phonon renormalization not only reduces the 3ph and 4ph scattering rates but also drags most of the ill-defined phonons back to become well-defined, especially for 4ph scatterings and at high temperatures, e.g., 1500 K (phonon scattering rates lower than Cahill's limit [59]) [see Figs. 4(e) and 4(f)]. This contributes to restoring the validity of particlelike phonon pictures by promoting the phonon MFPs [14]. More specifically, we found that both the 3ph and 4ph scattering rates within a low-frequency regime, i.e., ~2 and 4 THz for 3ph and 4ph scattering processes, respectively, exhibit a peculiar feature in Figs. 4(e) and 4(f), i.e., the phonon modes split into two separated portions. The phonon scattering rates in one part increase with increasing frequency, whereas those in the other part show an opposite trend. In the above landscape, the former part is contributed by the acoustic modes, and it follows the frequency dependence of $\Gamma_q^{3ph} \sim \omega^2$ and $\Gamma_q^{4ph} \sim \omega^\xi$, where $\xi > 2$, a typical feature of acoustic phonon modes for 3ph [44] and 4ph processes [58]. The latter derives from the phonons near the R_{25} modes, indicating the

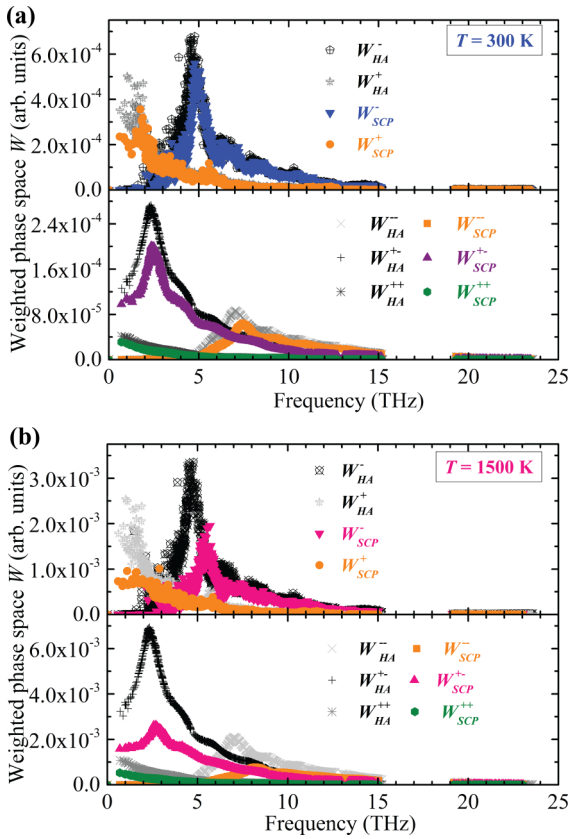

FIG. 5. (a) Calculated energy- and momentum-conserving phonon weighted phase space (WPS) using the harmonic approximation (HA)/self-consistent phonon (SCP)+3ph and HA/SCP+3,4ph models at $T = 300$ K, respectively, the superscripts $(+, -; ++, +-, --)$ of the WPS W denote the scattering processes, namely, the absorption $(\boldsymbol{q} + q' \rightarrow q'')$ and emission $(q \rightarrow q' + q'')$ processes for three-phonon scattering processes and the recombination $(q + q' + q'' \rightarrow q''')$, redistribution $(q + q' \rightarrow q'' + q''')$, and splitting $(q \rightarrow q' + q'' + q''')$ processes for four-phonon scattering processes. (b) The same as (a) but at $T = 1500$ K.

strong anharmonicity of the AFD mode, e.g., the R_{25} modes, as also observed in another perovskite $SrTiO_3$ [17]. Particularly, the phonon scattering rates of phonon modes around the R point are close to or larger than Cahill's limit within the HA theory; however, the anharmonic phonon renormalization significantly suppresses them and makes them well-defined at high temperatures [see Figs. 4(e) and 4(f)]. This phenomenon highlights the importance of proper treatment of strong anharmonic modes in the accurate prediction of κ_L^P in crystalline $BaZrO_3$ at elevated temperatures.

The magnitude of the 3ph and 4ph scattering rates is approximately proportional to the phonon WPS and the square of the scattering matrix elements (SSMEs) [47,50]. To shed light on the microscopic origin of the reduction in the 3ph and 4ph scattering rates, we calculated the WPS with the HA/SCP+3/3,4ph models at 300 and 1500 K, respectively, as shown in Figs. 5(a) and 5(b). Within the phonon frequency range of 0–2 THz, the reduction in the 3ph absorption processes W^+ dominates over the change of the total 3ph WPS induced by anharmonic phonon renormalization. By comparing the change in the 3ph scattering rates and the WPS, the suppression in the WPS induced by anharmonic phonon renormalization is sufficient to explain the reduction in 3ph scattering rates in the same frequency range, particularly for phonons near the R_{25} mode [see Figs. 4(e), 4(f), 5(a), and 5(b)]. Therefore, we attribute the reduction in phonon scattering rates to the reduced coupling between the acoustic and optical phonons within the frequency range of 0–2 THz. In addition, the suppression in the WPS of the 3ph emission processes W^- was also observed in the phonon frequency range of 2–6 THz, weakening the strong coupling between the transverse acoustic (TA)/longitudinal acoustic (LA) and TO phonons, e.g., phonons near the Γ_{15} mode [60]. This results in the reduction in 3ph scattering rates and enhances the spectral $\kappa_L^P(\omega)$ in the corresponding frequency interval. To reveal the role of the WPS in suppressing phonon scattering rates, we further quantitatively examined the SSMEs in two specific phonon modes, namely, the TA and R_{25} modes, using the harmonic and anharmonic phonon eigenvectors (see Figs. S8(a) and S8(b) in the SM [39]). As expected, we observed the negligible change in the SSMEs for both TA and R_{25} modes with increasing temperature, revealing that the reduction in WPS is responsible for the suppression in 3ph scattering rates and the enhancement in the spectral $\kappa_L^P(\omega)$.

We move on to unveil the origin of the reduction in the 4ph scattering rates induced by anharmonic phonon renormalization. As presented in Figs. 5(a) and 5(b), we observed the evident reduction of the 4ph redistribution process W^{+-} and splitting process W^{--} in the frequency ranges of 0–6 THz and 5–10 THz, respectively, when the phonons are anharmonically renormalized at finite temperatures. The magnitude of the reduction in 4ph WPS is consistent with the suppression of 4ph scattering rates induced by the anharmonically renormalized phonons in the same frequency range [see Figs. 4(e), 4(f), 5(a), and 5(b)]. Additionally, the 4ph SSMEs are of a minor effect on the change in phonon scattering rates because the phonon frequency shifts $(\nabla\omega)$ are not involved in the calculated SSMEs [47,50], which is verified for the 3ph scattering processes (see Figs. S8(a) and S8(b) in the SM [39]). Interestingly, the corresponding shifts in both the 3ph and 4ph WPSs are mainly contributed by strongly anharmonic low-frequency optical modes, i.e., the phonons in the vicinity of the Γ_{15}, M_3, and R_{25} modes due to their large phonon frequency increase, as indicated by the similar pace of the WPS shift and the phonon hardening [see Figs. 1(d), 5(a), and 5(b)]. Overall, the low-frequency optical phonon hardening, namely, the phonon frequency shifts near the Γ_{15}, R_{25}, and M_3 modes, significantly suppresses the 3ph and 4ph WPSs. The phonons with a frequency <6 THz, which are the major heat carriers, coexist with large 3ph and 4ph WPSs giving rise to the coupling between the acoustic and optical modes. The phonon renormalization dramatically weakens the coupling between the acoustic and optical modes in the low-frequency region and enhances the relative contribution of κ_L^P from acoustic phonons [see Figs. 4(c) and 4(d)].

Finally, we move on to analyze the coherent thermal transport channel resulting from the off-diagonal terms of the heat flux operators (wavelike interbranch tunneling of coherence), which is related to the lattice anharmonicity (phonon broadening) and phonon interbranch spacings [48,49,61]. Considering both the 3ph and 4ph scatterings, Fig. 6(a) shows that the

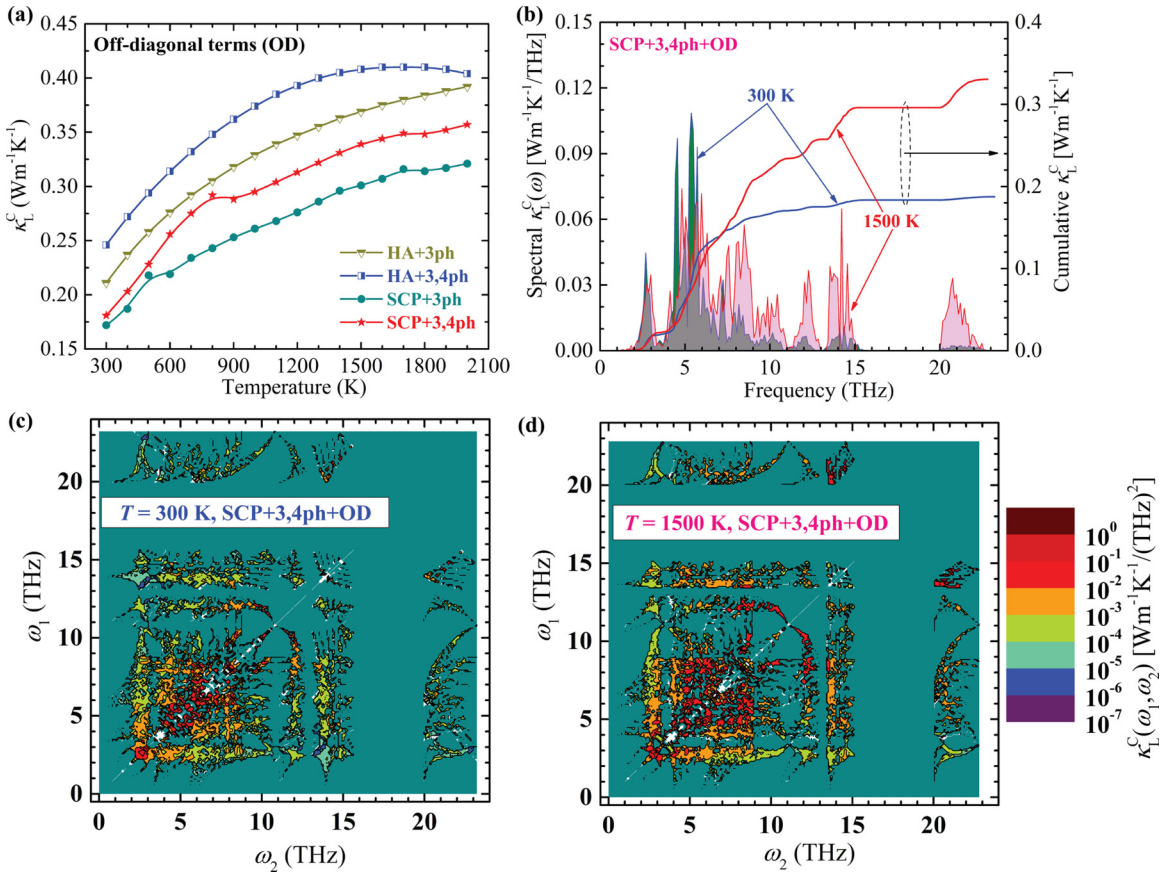

FIG. 6. (a) Temperature-dependent thermal conductivity of the interbranch coherence contribution κ_L^C calculated using the harmonic approximation (HA) and self-consistent phonon (SCP) frequencies and eigenvectors with/without considering four-phonon scattering processes, respectively. (b). The spectral and cumulative coherent thermal conductivity with SCP+3,4ph calculation at $T = 300$ and 1500 K, respectively. The contribution of phonon mode j in coherence couplings between two phonon modes $(\boldsymbol{q}, j)$ and $(\boldsymbol{q}, j')$ is calculated by $c_{qj}/(c_{qj} + c_{qj'})$, where c_{qj} is the phonon mode-specific heat. (c) Two-dimensional modal $\kappa_L^C(\omega_1, \omega_2)$ of the contribution to the thermal conductivity of interbranch coherent terms calculated using anharmonic phonon frequencies and eigenvectors and considering both the three- and four-phonon scattering processes at $T = 300$ K. The diagonal data points ($\omega_1 = \omega_2$) correspond to phonon degenerate eigenstates. (d) The same as (c) but $T = 1500$ K.

coherence contributions calculated by anharmonic phonon frequencies and eigenvectors contribute 2.68% to the total thermal conductivity κ_L of $BaZrO_3$ at 300 K. This small contribution can be attributed to its relatively sparse phonon branches despite the strong anharmonicity. As the temperature increases, the contribution of the coherence term becomes larger, e.g., 17.38% at 1500 K. Therefore, the coherent terms become nonnegligible at high temperatures and reduce the discrepancy between the predicted and measured results at elevated temperatures.

To better understand the impact of lattice anharmonicity including third and fourth orders on the coherent thermal transport channel, we further compare the coherence contributions obtained by the HA/SCP+3/3,4ph models, respectively. Figure 6(a) shows that the anharmonically renormalized phonons suppress the coherence contributions, which results from the reduction in the 3ph and 4ph scattering rates [see Figs. 4(e) and 4(f)]. In contrast, further considering 4ph scattering processes enhances the coherence contributions due to the enhancement in phonon broadening (phonon scattering rates). To get deep insight into the microscopic mechanism of the coherent thermal transport channel, we calculated the spectral contribution to the coherent thermal conductivity $\kappa_L^C(\omega)$ using the SCP+3,4ph model, as plotted in Fig. 6(b). Figure 6(b) shows that the phonon modes within 4–10 THz contribute most to the coherent terms due to relatively dense phonon branches in this region. In addition, it also reveals that almost all the low-frequency modes <7 THz are excited at 300 K. Figure 6(c) shows that the couplings between the phonon quasidegenerate states ($\omega_1 \cong \omega_2$) mainly contribute to the coherent terms at 300 K. However, in addition to the quasidegenerate state contributions, the couplings between phonon modes with very different frequencies, e.g., 6/8 THz, 10/12 THz, and 14/21 THz, account for a noticeable contribution at 1500 K due to stronger anharmonicity of high-frequency phonon modes and high-frequency-phonon-mode excitation at high temperatures [see Figs. 6(b) and 6(d)]. We note that the coherence contributions of simple crystalline $BaZrO_3$ do not dominate the total thermal conductivity like complex compounds $CsPbBr_3$ [23] and $Cu_{12}Sb_4S$ [16], but it becomes more and more important at high temperatures in this highly anharmonic material.

To this end, using the highest level of thermal transport theory in this paper, i.e., the SCP+3,4ph+OD model, our

current theoretical results successfully uncover the microscopic mechanisms of thermal transport in cubic perovskite $BaZrO_3$ over a wide range of temperatures. However, the current κ_L may be improved by further considering the following factors: (i) thermal expansion with increasing temperature and (ii) adding up the anharmonic contributions of heat flux operators.

IV. CONCLUSIONS

In summary, we have performed *ab initio* calculations to investigate the lattice dynamics and microscopic mechanisms of thermal transport in crystalline $BaZrO_3$ by considering the anharmonic phonon renormalization induced by both the cubic and quartic anharmonicities, 3ph and 4ph scattering processes, and coherent thermal transport channel. In this paper, all the phonon frequency shifts induced by bubble (cubic anharmonicity) and loop diagrams (quartic anharmonicity) were evaluated in a nonperturbative manner (SCP) instead of a perturbative manner due to the large phonon hardening of low-frequency optical modes. Our results show that the low-frequency optical modes corresponding to weak antiparalleled motions between oxygen ions and cations (Ba and Zr) and ZrO_6 octahedra tilting exhibit strong anharmonicity due to the associated large MSD of O atoms and deep-flat U-shaped PESs. Anharmonic phonon renormalization results in notable phonon hardening of strongly anharmonic low-frequency optical phonons and phonon softening in the high-frequency regime stemming from the competition between the phonon hardening from the quartic anharmonicity and phonon softening from the cubic anharmonicity. The anharmonic phonon renormalization remarkably increases the predicted values of thermal conductivity κ_L relative to the conventional HA. This enhancement is mainly due to the phonon hardening of low-frequency phonons, which drastically reduces the 3ph and 4ph scattering rates by suppressing the phonon WPS of the low-frequency phonon modes. The optical modes dominate the thermal transport of crystalline $BaZrO_3$ over a wide range of temperature, whereas the acoustic modes play an essential role in enhancing the total κ_L. Moreover, the strongly anharmonic low-frequency optical modes exhibit strong coupling with the acoustic phonons, leading to the low κ_L in crystalline $BaZrO_3$. The coherence contributions to the total thermal conductivity κ_L are negligible at low temperatures due to the sparse phonon branches in the simple cubic structure of $BaZrO_3$; however, they become nonnegligible at elevated temperatures due to large 3ph and 4ph scattering rates and high-frequency phonon excitation. These findings highlight the importance of proper treatment of lattice anharmonicity, i.e., cubic and quartic anharmonicity, in precisely modeling lattice dynamics and thermal transport in materials with strong anharmonicity.

ACKNOWLEDGMENTS

We are thankful for the financial support from the Science and Technology Planning Project of Guangdong Province, China (Grant No. 2017A050506053), the Science and Technology Program of Guangzhou (No. 201704030107), and the Hong Kong General Research Fund (Grants No. 16214217 and No. 16206020). This work was supported in part by the Project of Hetao Shenzhen-Hong Kong Science and Technology Innovation Cooperation Zone (HZQB-KCZYB-2020083). R.G. acknowledges support from the Excellent Young Scientists Fund (Overseas) of Shandong Province (2022HWYQ-091) and the Initiative Research Fund of Shandong Institute of Advanced Technology (2020107R03). We are also thankful for the fruitful discussions with Changpeng Lin from École Polytechnique Fédérale de Lausanne.

[1] R. B. Wexler, G. Sai Gautam, E. B. Stechel, and E. A. Carter, J. American Chemical Society **143**, 13212 (2021).
[2] P. S. Dobal, A. Dixit, R. S. Katiyar, Z. Yu, R. Guo, and A. S. Bhalla, J. Appl. Phys. **89**, 8085 (2001).
[3] A. Azad, S. Subramaniam, and T. W. Dung, J. Alloys Compd. **334**, 118 (2002).
[4] E. Celik, Y. Akin, I. H. Mutlu, W. Sigmund, and Y. S. Hascicek, Physica C **382**, 355 (2002).
[5] C. Duan, R. Kee, H. Zhu, N. Sullivan, L. Zhu, L. Bian, D. Jennings, and R. O'Hayre, Nat. Energy **4**, 230 (2019).
[6] K. Kreuer, Annu. Rev. Mater. Res. **33**, 333 (2003).
[7] I. Sato, H. Furuya, T. Arima, K. Idemitsu, and K. Yamamoto, J. Nucl. Sci. Technol. **36**, 775 (1999).
[8] X. Q. Cao, R. Vassen, and D. Stöver, J. Eur. Ceram. Soc. **24**, 1 (2004).
[9] R. Vassen, X. Cao, F. Tietz, D. Basu, and D. Stöver, J. Am. Ceram. Soc. **83**, 2023 (2000).
[10] K. Kurosaki, J. Adachi, T. Maekawa, and S. Yamanaka, J. Alloys Compd. **407**, 49 (2006).
[11] Y. Liu, W. Zhang, B. Wang, L. Sun, F. Li, Z. Xue, G. Zhou, B. Liu, and H. Nian, Ceram. Int. **44**, 16475 (2018).
[12] S. Yamanaka, K. Kurosaki, T. Maekawa, T. Matsuda, S. Kobayashi, and M. Uno, J. Nucl. Mater. **344**, 61 (2005).
[13] A. van Roekeghem, J. Carrete, C. Oses, S. Curtarolo, and N. Mingo, Phys. Rev. X **6**, 041061 (2016).
[14] Y. Xia, K. Pal, J. He, V. Ozoliņš, and C. Wolverton, Phys. Rev. Lett. **124**, 065901 (2020).
[15] T. Tadano and S. Tsuneyuki, Phys. Rev. Lett. **120**, 105901 (2018).
[16] Y. Xia, V. Ozoliņš, and C. Wolverton, Phys. Rev. Lett. **125**, 085901 (2020).
[17] T. Tadano and S. Tsuneyuki, Phys. Rev. B **92**, 054301 (2015).
[18] T. R. Koehler, Phys. Rev. Lett. **17**, 89 (1966).
[19] T. Tadano and W. A. Saidi, arXiv:2103.00745.
[20] O. Hellman, I. A. Abrikosov, and S. I. Simak, Phys. Rev. B **84**, 180301 (2011).
[21] G. P. Srivastava, *The Physics of Phonons* (Routledge, New York, 2019).
[22] S. Mukhopadhyay, D. S. Parker, B. C. Sales, A. A. Puretzky, M. A. McGuire, and L. Lindsay, Science **360**, 1455 (2018).
[23] M. Simoncelli, N. Marzari, and F. Mauri, Nat. Phys. **15**, 809 (2019).
[24] T. Trautmann and C. Falter, J. Phys. Condens. Matter **16**, 5955 (2004).

[25] V. Železný, E. Cockayne, J. Petzelt, M. F. Limonov, D. E. Usvyat, V. V. Lemanov, and A. A. Volkov, Phys. Rev. B **66**, 224303 (2002).
[26] S. Glinšek, D. Nuzhnyy, J. Petzelt, B. Malič, S. Kamba, V. Bovtun, M. Kempa, V. Skoromets, P. Kužel, and I. Gregora, J. Appl. Phys. **111**, 104101 (2012).
[27] P. Hohenberg and W. Kohn, Phys. Rev. **136**, B864 (1964).
[28] G. Kresse and J. Furthmüller, Phys. Rev. B **54**, 11169 (1996).
[29] P. E. Blöchl, Phys. Rev. B **50**, 17953 (1994).
[30] J. P. Perdew, K. Burke, and M. Ernzerhof, Phys. Rev. Lett. **77**, 3865 (1996).
[31] J. P. Perdew, K. Burke, and Y. Wang, Phys. Rev. B **54**, 16533 (1996).
[32] A. R. Akbarzadeh, I. Kornev, C. Malibert, L. Bellaiche, and J. Kiat, Phys. Rev. B **72**, 205104 (2005).
[33] A. Perrichon, E. Jedvik Granhed, G. Romanelli, A. Piovano, A. Lindman, P. Hyldgaard, G. Wahnström, and M. Karlsson, Chem. Mater. **32**, 2824 (2020).
[34] S. Baroni, S. De Gironcoli, A. Dal Corso, and P. Giannozzi, Rev. Mod. Phys. **73**, 515 (2001).
[35] R. A. Evarestov, Phys. Rev. B **83**, 014105 (2011).
[36] K. Esfarjani and H. T. Stokes, Phys. Rev. B **77**, 144112 (2008).
[37] E. J. Candès and M. B. Wakin, IEEE Signal Process. Mag. **25**, 21 (2008).
[38] L. J. Nelson, G. L. Hart, F. Zhou, and V. Ozoliņš, Phys. Rev. B **87**, 035125 (2013).
[39] See Supplemental Material at http://link.aps.org/supplemental/10.1103/PhysRevB.105.224303 for temperature-dependent bond strengths, phonon dispersions, atomic participation ratio, phonon frequency shift, phonon MFP, total phonon scattering rates, and scattering matrix elements.
[40] R. A. Cowley, W. Buyers, and G. Dolling, Solid State Commun. **7**, 181 (1969).
[41] K. 'Otnes, T. Riste, G. Shirane, and J. Feder, Solid State Commun. **9**, 1103 (1971).
[42] N. Lehner, H. Rauh, K. Strobel, R. Geick, G. Heger, J. Bouillot, B. Renker, M. Rousseau, and W. G. Stirling, J. Phys. C: Solid State Phys. **15**, 6545 (1982).
[43] T. Tadano and S. Tsuneyuki, J. Phys. Soc. Jpn. **87**, 041015 (2018).
[44] T. Tadano, Y. Gohda, and S. Tsuneyuki, J. Phys. Condens. Matter **26**, 225402 (2014).
[45] M. Omini and A. Sparavigna, Physica B **212**, 101 (1995).
[46] M. Omini and A. Sparavigna, Phys. Rev. B **53**, 9064 (1996).
[47] Z. Han, X. Yang, W. Li, T. Feng, and X. Ruan, Comput. Phys. Commun. **270**, 108179 (2022).
[48] R. J. Hardy, Phys. Rev. **132**, 168 (1963).
[49] P. B. Allen and J. L. Feldman, Phys. Rev. B **48**, 12581 (1993).
[50] W. Li, J. Carrete, N. A. Katcho, and N. Mingo, Comput. Phys. Commun. **185**, 1747 (2014).
[51] M. A. Helal, T. Mori, and S. Kojima, Appl. Phys. Lett. **106**, 182904 (2015).
[52] D. Nuzhnyy, J. Petzelt, M. Savinov, T. Ostapchuk, V. Bovtun, M. Kempa, J. Hlinka, V. Buscaglia, M. T. Buscaglia, and P. Nanni, Phys. Rev. B **86**, 014106 (2012).
[53] C. Toulouse, D. Amoroso, C. Xin, P. Veber, M. C. Hatnean, G. Balakrishnan, M. Maglione, P. Ghosez, J. Kreisel, and M. Guennou, Phys. Rev. B **100**, 134102 (2019).
[54] P. Chen, M. N. Grisolia, H. J. Zhao, O. E. González-Vázquez, L. Bellaiche, M. Bibes, B. Liu, and J. Íñiguez, Phys. Rev. B **97**, 024113 (2018).
[55] J. N. Bull, W. C. Tennant, T. B. Ballaran, F. Nestola, and C. A. McCammon, Phys. Chem. Miner. **39**, 561 (2012).
[56] S. Wang, H. Yan, D. Zhao, Z. Tan, and Q. Shi, J. Chem. Thermodyn. **158**, 106449 (2021).
[57] T. Sun and P. B. Allen, Phys. Rev. B **82**, 224305 (2010).
[58] T. Feng, L. Lindsay, and X. Ruan, Phys. Rev. B **96**, 161201 (2017).
[59] D. G. Cahill, S. K. Watson, and R. O. Pohl, Phys. Rev. B **46**, 6131 (1992).
[60] L. Feng, T. Shiga, and J. Shiomi, Appl. Phys. Express **8**, 071501 (2015).
[61] D. C. Knauss and R. S. Wilson, Phys. Rev. B **10**, 4383 (1974).